POLLUTANT REMOVAL AND THE HEALTH EFFECTS OF ENVIRONMENTAL POLLUTION

Check for updates

Nanosheets- and nanourchins-like nanostructures of MoSe₂ for photocatalytic water purification: kinetics and reusability study

Honey Mittal[1] · Manika Khanuja[1]

Abstract

In this paper, we are reporting a simple hydrothermal technique for preparation of $MoSe_2$ nanostructures (nanourchins and nanosheets) using selenium and sodium molybdate as precursors. Samples are characterized by field emission scanning electron microscopy (FESEM), X-ray diffraction (XRD), Raman spectroscopy, UV-Vis spectroscopy, Brunauer-Emmett-Teller (BET), and X-ray photoelectron spectroscopy (XPS). The FESEM revealed that the morphology of materials was varying significantly by changing pH value during synthesis. Photocatalytic degradation of anionic dye (MO), cationic dye (MB), and reduction of Cr(VI) into Cr(III) were performed. Nanosheets and nanourchins showed higher photocatalytic activity, enhanced photocatalytic degradation efficiency is correlated with the higher ˙OH radical concentration, crystallinity of material, and large surface area as evident through XPS, XRD, and BET, respectively. Photocatalysis mechanism along with role of reactive species (˙OH and holes) were explained using trapping experiments. Identification of degraded products was carried out using high-performance liquid chromatography (HPLC). Reaction kinetics and reusability of materials were also studied; wherein, it was observed that the materials have reusable properties.

Introduction

Increasing number of contaminants such as heavy metal ions, dyes, and organic chemicals in natural water is dangerous to environment and humans. Cr(VI) and dyes are common contaminants which are discharged from industries to water bodies. They are highly dissolvable in water and can cause lung cancer, intestine cancer, kidney damage, asthma, etc. (Ashraf et al. 2019) (Shrivastava 2012; Singh et al. 2017; Toor and Jin 2012). Photocatalysis has been proved to be a capable method to remove water contaminants due to low cost, low energy consumption, and regenerable solution (Bhuyan et al. 2015; Salem et al. 2009; Sharma et al. 2017; Singh et al. 2018). Transition metal dichalcogenides (MoS_2, $MoSe_2$, WS_2, WSe_2) have enticed great attention due to special-layered stable structure, high carrier mobility, direct bandgap, large

surface area, and controllable interfaces (Andoshe et al. 2015; Saha et al. 2019; Wang et al. 2018). Among TMD's, $MoSe_2$ has been proved to be an efficient photocatalyst due to high surface activity, enormous surface area, good chemical stability, and visible-NIR region bandgap (Chu et al. 2016; Narang et al. 2018a; Siddiqui et al. 2018).

There are various methods to synthesize $MoSe_2$ nanostructures (in synthesis section—Table 1, various $MoSe_2$ synthesis methods are summarized) such as solvothermal, molecular beam epitaxy, electrochemical deposition, and chemical vapor deposition (Chu et al. 2016; Jia et al. 2015; Roy et al. 2016; Wang et al. 2016). These methods are complicated or require high temperatures to operate. Hydrothermal is a simple, environmentally friendly, and effective method to synthesize $MoSe_2$ nanostructures. Hydrothermal method provides controlled growth rate and nucleation uniformity, and it is suitable for large scale production (Chaudhary et al. 2018; Narang et al. 2018b). $MoSe_2$ exists in several crystal structures depending on the composition and temperature of the system; these structures exhibit diverse chemical and catalytic properties (Chu et al. 2016; Liu et al. 2015; Siddiqui et al. 2018; Fan et al. 2014).

Photocatalytic degradation process takes place at the interface between photocatalyst surface and pollutant; therefore, it is expected that the photocatalytic activity is correlated with

---

Responsible editor: Suresh Pillai

✉ Manika Khanuja
   manikakhanuja@gmail.com

[1] Centre for Nanoscience and Nanotechnology, Jamia Millia Islamia, New Delhi 110025, India

Table 1 Synthesis methods of MoSe$_2$ and comparison with respect to different parameters

Morphology of MoSe$_2$	Synthesis route	Precursors	Synthesis conditions	Size	References
Nano-flakes	Microwave-assisted polyol method	Na$_2$MoO$_4$, NH$_2$OH·HCl, ethanol, Cyanex 301 and NaHSe	70 °C for 3 h	Diameter ~ 70 nm	(Shi et al. 2008)
Porous microspheres	Colloidal route	MoCl$_5$, SeO$_2$, OAM	300 °C for 60 min	Diameter ~ 400–600 nm	(Zhang et al. 2015)
Nanosheets	Colloidal route	MoO$_2$, oleylamine and ethanol	240 °C for 20 min	Thickness ~ 0.7 nm	(Zhou et al. 2014)
Nanosheets	Hydrothermal (in presence of CTAB)	(NH$_4$)$_6$Mo$_7$O$_{24}$, Se, N$_2$H$_4$ · H$_2$O and CTAB	200 °C for 10 h	2–3 layers	(Wu et al. 2016)
Snow-like	Chemical vapor deposition (CVD)	MoO$_3$, Se	820 °C for 15 min	Thickness ~ 0.9 nm	(Huang et al. 2017)
Nanoflowers	Hydrothermal	Na$_2$MoO$_4$, N$_2$H$_4$ · H$_2$O and Se	200 °C for 48 h	Diameter ~ 100 nm	(Fan et al. 2014)
Nanorods	Microwave assisted Polyol	Se, Mo (CO)$_6$, and ethylene glycol	135 °C for 12 h.	lengths ~ 45–55 nm	(Harpeness et al. 2003)
Nanoflowers	Phosphine-free solution-processing	Na$_2$MoO$_4$, oleic acid, 1-Octadecene, 1-Octylamine, Se and S	300 °C	Diameter ~ 250 nm	(Zhang et al. 2018)
Yolk–shell microspheres	Selenization process	MoO$_3$, hydrogen selenide vapor	300 °C for 24 h	Thickness ~ 10 nm	(Ko et al. 2014)
Broom-shaped	Hydrothermal	Na$_2$MoO$_4$, N$_2$H$_4$ · H$_2$O and Se	200 °C for 24 h	length ~ 10 μm and diameter ~ 150 nm	(Siddiqui et al. 2018)
Plate shaped	Solvothermal	MoO$_3$, N$_2$H$_4$.H$_2$O, and Se	300 °C for 12 h	Diameter ~ 40 nm	(Zhan et al. 1999)
Nanoislands nanoribbons	Molecular beam epitaxy	Mo and Se	500 °C 650 °C	Height ~ 0.8 nm Average width ~ 15 nm	(Poh et al. 2017)
Nanosheets and Nanourchins	Hydrothermal	Na$_2$MoO$_4$, N$_2$H$_4$ · H$_2$O and Se	200 °C for 24 h	Diameter ~ 150 nm	This work

crystalline planes and surface structures. $^{•}$OH radical is a major reactant responsible for the photocatalytic degradation of pollutants. $^{•}$OH radicals are formed on MoSe$_2$ surface when holes react with adsorbed water, and electrons react with oxygen-forming superoxide radical which further react and form $^{•}$OH radicals. Researchers reported that there is a direct correlation between the amount of $^{•}$OH generation and photocatalytic efficiency (Gągol et al. 2018). Acidic conditions promote the generation of hydroxyl radicals by lowering the recombination reaction of hydroxyl radicals.

It was observed from previously reported results, MoSe$_2$ is a good photocatalyst for cationic dyes such as methylene blue (MB) and rhodamine B (RhB) (Wu et al. 2016). For degradation of anionic dye, surface modification of MoSe$_2$ is required which is possible via doping, synthesizing composite with other suitable materials, and varying pH (Zhou et al. 2018). In this study, nanosheets and nanourchins of MoSe$_2$ were hydrothermally synthesized by varying the pH and comparative photocatalytic study on organic dyes (MB, MO) and heavy metal Cr(VI) were performed. Enhanced photocatalytic efficiency of nanosheets over nanourchins is observed and is correlated with crystallinity, enhanced surface area, and hydroxyl ion concentration. Adsorption studies, role of reactive

species, intermediate products using HPLC, and regenerable properties of catalysts were also studied.

Materials

MilliQ deionized water (DI) was used as base-liquid. Selenium Se (99.99%), Central Drug House Pvt. Ltd., sodium molybdate, Na$_2$MoO$_4$ (99.99%), Thermo Fisher Scientific India Pvt. Ltd., hydrazine hydrate, N$_2$H$_4$.H$_2$O (80%), Central Drug House Pvt. Ltd. and acetic acid, CH$_3$COOH (99.5%) from High Purity Laboratory Chemicals Pvt. Ltd. solutions were used in synthesis. Methylene blue (C$_{16}$H$_{18}$ClN$_3$S, Fisher scientific), methyl orange (C$_{14}$H$_{14}$N$_3$NaO$_3$S, Fisher scientific), potassium iodide (KI, Pallav chemicals and solvents Pvt. Ltd.), and tert-butyl alcohol ((CH$_3$)$_3$COH, Central Drug House Pvt. Ltd.) have been used for photocatalysis.

Synthesis process

Schematic of synthesis process for MoSe$_2$ nanostructures (nanosheets and nanourchins) is shown in Fig. 1. Two solutions are prepared, in the first solution, 0.02 mol of sodium
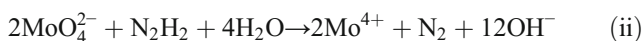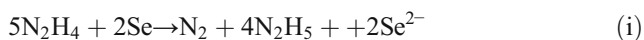
Fig. 1 Schematic of MoSe$_2$ (nanosheets and nanourchins) synthesis process
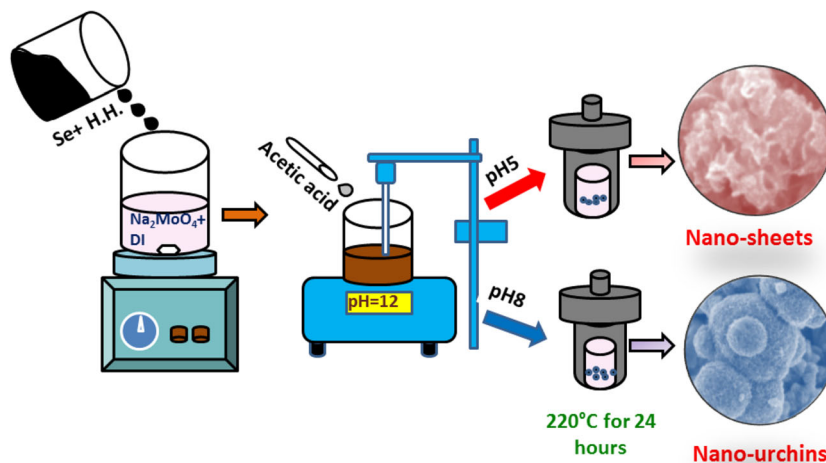
molybdate is dissolved in 50 ml of deionized water (DI) at room temperature and stirred until clear solution is obtained. Separately, second solution is prepared by dissolving 0.04 mol of selenium powder in 10 ml of hydrazine hydrate at room temperature and stirred, to give complete black suspension. Selenium reacts with hydrazine hydrate to yield selenium ions (Se^{2-}) as shown in Eq. (i). Second solution is added dropwise to the first solution and stirred for 20 min. Hydrazine hydrate reduces MoO$_4^{2-}$ anions from sodium molybdate and produce Mo^{4+} cations, as shown in Eq. (ii). The resultant dark brown color solution is obtained with pH 12.

MoSe$_2$ nanostructure at pH 5 and pH 8

Acetic acid is added to the as-prepared solution of pure MoSe$_2$ (before transferring to autoclave) to change the pH value of the solution. Solutions at pH 5 and pH 8 were obtained by adding 13 ml and 6 ml of acetic acid, respectively. Finally, dark brown color solutions were transferred to autoclave and placed in furnace at 200 °C for 24 h. In autoclave, reaction between Se^{2-} and Mo^{4+} takes place to form MoSe$_2$ as shown in Eq. (iii) (Mittal et al. 2019). After 24 h, the autoclaves are allowed to cool till room temperature. Subsequently, obtained solutions were sequentially washed with DI water and acetone, followed by drying at 50 °C for 2 h. Samples prepared at pH 5 and pH 8 are labelled as MSE5 and MSE8, respectively.

$$5N_2H_4 + 2Se \rightarrow N_2 + 4N_2H_5 + +2Se^{2-} \tag{i}$$

$$2MoO_4^{2-} + N_2H_2 + 4H_2O \rightarrow 2Mo^{4+} + N_2 + 12OH^- \tag{ii}$$

$$Mo^{4+} + 2Se^{2-} \rightarrow MoSe_2 \tag{iii}$$

Relevant synthesis condition, raw materials, size, and morphology of Mose$_2$ are summarized in Table 1. In the present study, we have reported synthesis of nanosheets and nanourchins morphology of MoSe$_2$ using simple and economic hydrothermal method.

Characterizations

FESEM (Quanta 3D FEG) analysed the morphology of the powdered MoSe$_2$. Crystal structure was analysed using XRD (Rigaku Smart Lab) with Cu K$_\alpha$ radiation of 1.540 Å in the range of 10–80°. UV-Vis spectrophotometer (Cary 100 series, Agilent Technologies) was used to analyse the band gap of the synthesized materials. Raman spectroscopy (HR800 JY, Lab RAM HR) was carried out in the range of 220 to 300 cm^{-1}. XPS (Multiprobe Surface analysis system, Omicron) was used to determine the hydroxyl ion concentration. The surface areas and pore diameter of the materials were analyzed using multipoint BET and Barrett-Joyner-Halenda (BJH) method by nitrogen adsorption–desorption isotherm measurements at 77.4 K using Quantachrome Instruments (version 3.0). The degradation products of MB were analysed by HPLC (Agilent technologies (1260- ∞ series)) using Hiplex X Column with temperature of detector and column at 35 °C and 65 °C, respectively. Deionized water was used as mobile phase with flow rate of 0.6 ml/min.

Results and discussion

Morphology of as synthesized materials was studied using FESEM as shown in Fig. 2. Figure 2a–d showed the SEM images of MSE5 and MSE8 at magnification of 1 μm and 100 nm. MSE5 showed clusters of nanosheets, the pattern is irregular, inner surface is dense, and smooth while the outer surface is composed of multiple folds nanosheets. MSE8 consists of evenly circulated microsphere of diameter ~ 150 nm. The nanourchins were made by the accumulation of several nanospheres which were gathered at one place and giving

Fig. 2 FESEM images of MoSe$_2$ of **a**, **b** nanosheets and **c**, **d** nanourchins at 1 μm and 100 nm
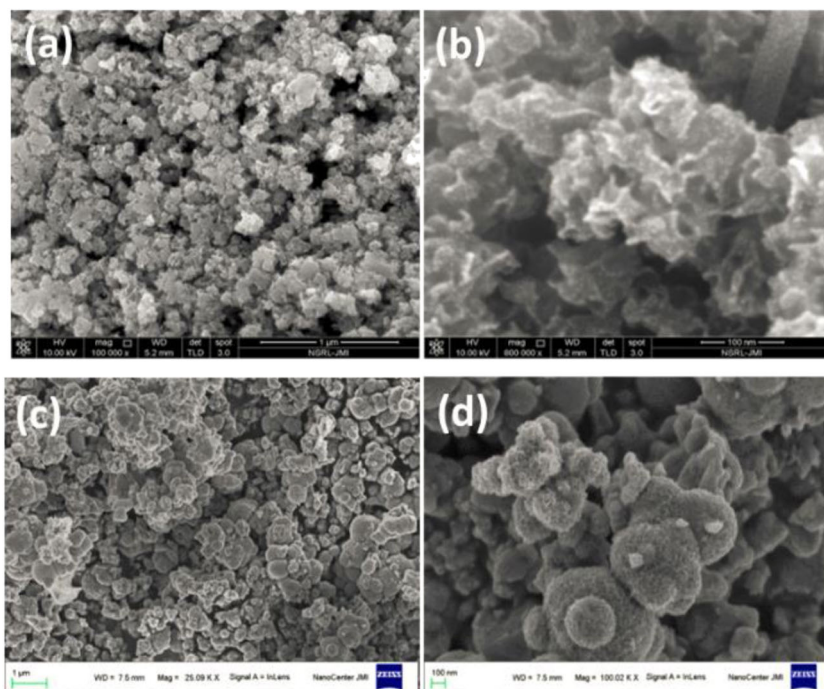
realization of nanourchins. Thus, significant change in morphology was observed by changing synthesis conditions.

Crystal structure and orientation of MSE5 and MSE8 were observed by XRD diffractograms as shown in Fig. 3a and b, respectively. XRD peaks for MSE5 and MSE8 were observed at 2θ 13.6°, 13.4°; 26.3°, 26.1°; 31.3°, 31.5°; 37.8°, 37.7°; 46.8°,47.1°; 55.8°,55.9°, and 64.5°, 64.3° corresponds to (002), (100), (004), (102), (200), (211), and (204) hkl planes, respectively as confirmed by the JCPDS file no. 77-1715 (Roy et al. 2016; Saha et al. 2019; Tang et al. 2016). As observed from XRD, MSE5 has sharp and intense peaks as compared

with MSE8, implying higher crystallinity in MSE5 sample as compared with MSE8. The calculated lattice constants a and c were 3.3 Å and 12.56 Å for MSE5 and 3.3 Å and 12.9 Å for MSE8, which are in good agreement with the earlier results (Zhang et al. 2018).

To further confirm the crystallinity and phase components of MSE5 and MSE8, Raman spectra were recorded as shown in Fig 4a and b, respectively. In the Raman spectrum of MSE5, the peaks were positioned at 239.6 cm^{-1} and 284.8
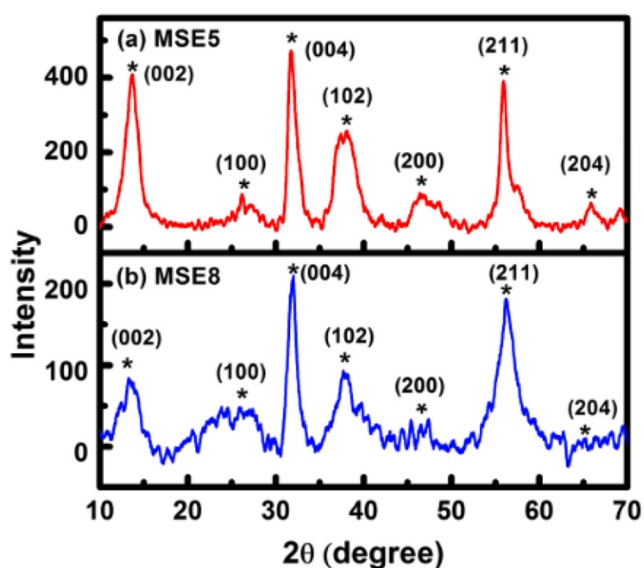
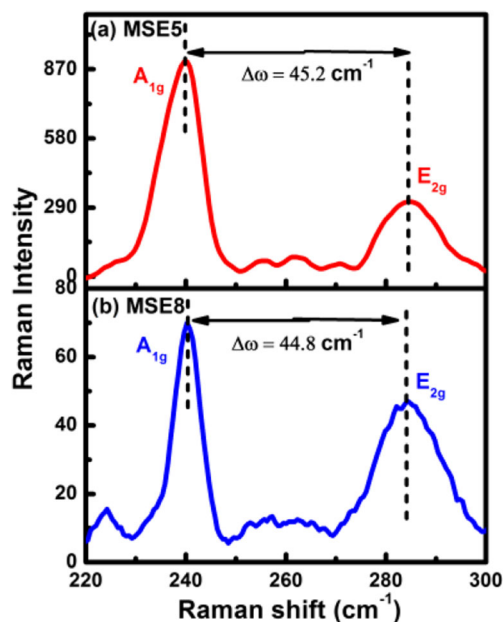

Fig. 3 XRD Diffractograms of **a** MSE5 and **b** MSE8
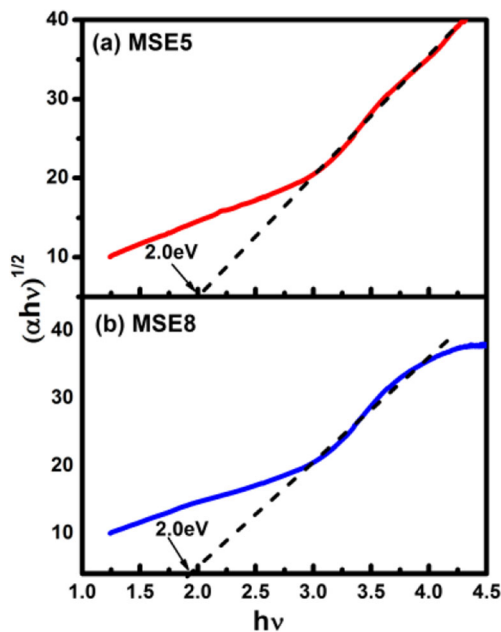

Fig. 4 Raman spectra of **a** MSE5 and **b** MSE8

Fig. 5 Tauc's plot of **a** MSE5 and **b** MSE8

Table 2 BET pore volume, pore diameter, and surface area for $MoSe_2$ nanostructures

Sample	Pore volume (cc/g)	Pore diameter (nm)	Surface area(m^2/g)
MSE5	0.246	8.178	78.63
MSE8	0.120	3.551	72.98

absorbance and t is the thickness of cuvette. It was observed that there is no effect of pH on band gap of $MoSe_2$.

The measurements of N_2 adsorption–desorption was performed to calculate the pore diameter, specific surface area, and the pore volume. One hundred milligram of MSE5 and MSE8 were degassed for 6 h at 150 °C before measurement and outgassed for 1 h at 100 °C. The nitrogen adsorption–desorption isotherms and pore size distribution obtained for MSE5 and MSE8 are shown in Fig. 6a and b, respectively. Table 2 represented the BET surface area and pore diameter of MSE5 and MSE8. MSE5 and MSE8 exhibit isotherm of type IV which is characteristic of mesoporous material. MSE8 has narrow pore size distributions than MSE5 and possessed a single peak which confirms uniform size distribution. BET surface area for MSE5 and MSE8 were 78.633 m^2 g^{-1} and 72.978 m^2 g^{-1}, respectively. The maximum pore size of MSE5 is 1.6 nm and of MSE8 is 3.5 nm which further confirms the mesoporous nature of MSE5 and MSE8.

XPS study was performed to confirm the oxidation state and calculate the hydroxyl ion concentration of synthesized materials (Khanuja et al. 2007; Khanuja et al. 2008). The general scan as shown in Fig. 7a and b indicated the elemental peaks of Mo, Se, C, and O. The HR-XPS of the Mo 3d core level of $MoSe_2$ are shown in Fig 7c and d, peak at 228.4 eV in MSE5 and 232.4 eV in MSE8 corresponded to Mo $3d_{5/2}$ and peak at 231.6 eV in MSE5 and 235.5 eV in MSE8 corresponded to Mo $3d_{3/2}$, suggesting Mo^{4+} characteristics (Zhao et al. 2016). As shown in Fig. 7e and f, Se $3d_{5/2}$ and
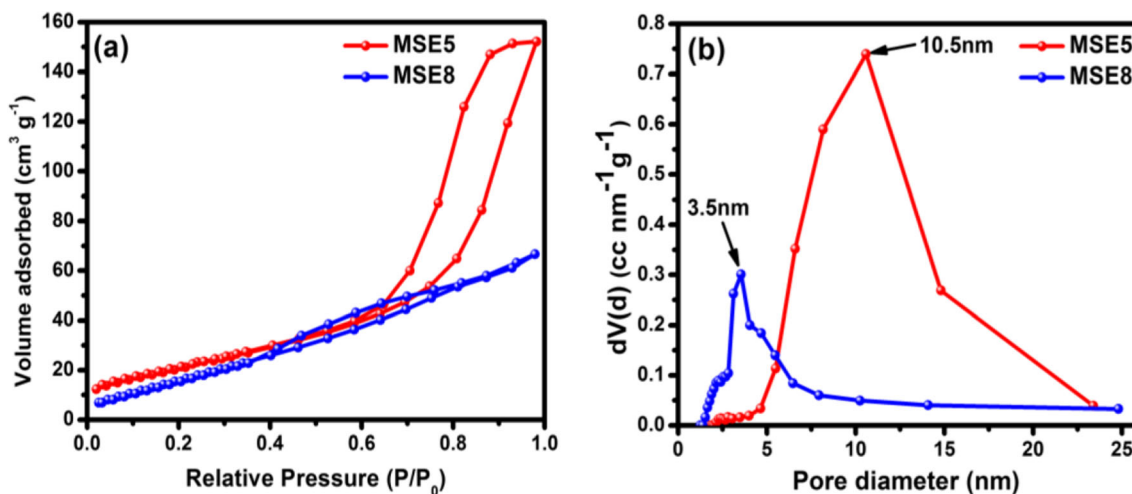
cm^{-1} and of MSE8, peaks positioned at 240.2 cm^{-1} and 284.9 cm^{-1}, corresponded to A_{1g} and E_{2g} phonon modes of $MoSe_2$, respectively (Ghosh et al. 2016; Kirubasankar et al. 2019). A_{1g} mode is assigned to out of plane and E_{2g} is assigned to in plane optical branch. The $\Delta\omega$ between E_{2g} and A_{1g} mode was 45.2 cm^{-1} and 44.8 cm^{-1} for MSE5 and MSE8, respectively. It was observed that MSE5 has high intensity as compared with MSE8 which implies more defects in MSE8 than in MSE5.

Band gap of MSE5 and MSE8 was calculated using Tauc'c plot as shown in Fig. 5a and b, respectively. Absorption spectra of MSE5 and MSE8 lie in the visible and IR region. Band gap energies were calculated from plot of $(\alpha h)^{1/2}$ vs h and found to be 2.0 eV for MSE5 and MSE8, where α is absorption coefficient, defined as $a = 2.303\ A/t$, where "A" is

Fig. 6 **a** Plot of N_2 adsorption–desorption isotherm and **b** pore-size distribution curves for MSE5 and MSE8
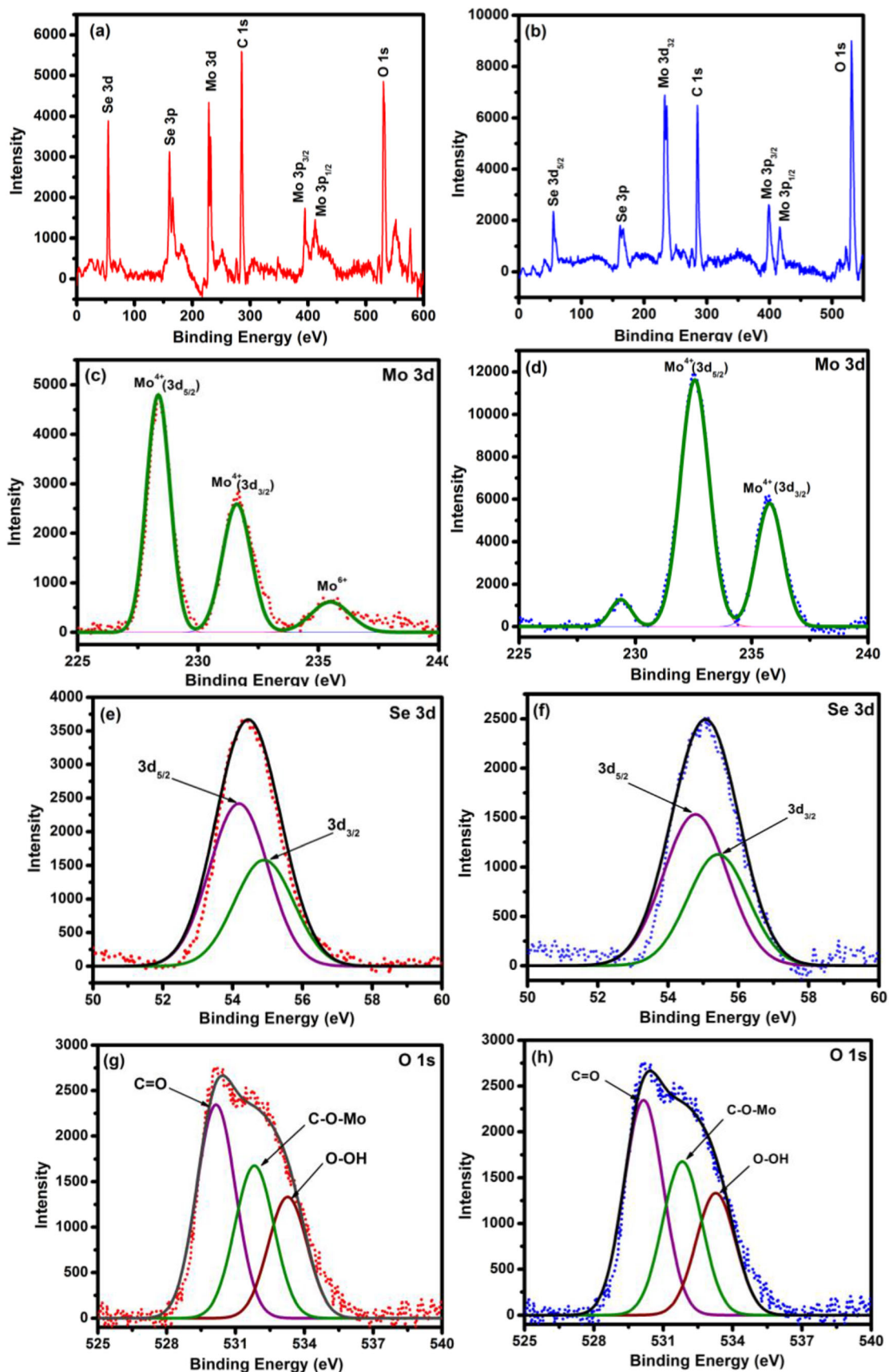
Fig. 7 XPS Spectra of **a**, **b** general scan; **c**, **d** Mo 3d; **e**, **f** Se 3d; and **g**, **h** O 1 s of MSE5 and MSE8

Se $3d_{3/2}$ components located at binding energies of 54.2 and 54.7 eV, respectively in MSE5 and 54.8 and 55.3 eV in MSE8, representing an oxidation state of − 2 for Se, thus confirmed the formation of $MoSe_2$ (Bi et al. 2015). The difference in binding energy because of the spin orbital coupling, $\Delta E_b = E_b$ (Se $3d_{3/2}$) − E_b (Se $3d_{5/2}$) was 0.5 eV. The O 1 s spectra are as shown in Fig. 7g and h, peaks at binding energy of 530.1 eV in MSE5 and 530.5 eV in MSE8 corresponded to C=O of $MoSe_2$, peak at 531.8 eV in MSE5 and 531.7 eV in MSE8 corresponded to the C–O–Mo and peak at 533.27 eV in MSE5 and 533.2 eV in MSE8 corresponded to O–OH (Azeez et al. 2018). Effect of pH was observed on surface hydroxyl concentration; percentage of hydroxyl oxygen concentration was 31.3% and 28.2% for MSE5 and MSE8, respectively. Hydroxyl radicals are responsible for degradation of pollutants, and increase in hydroxyl concentration was observed with decrease in pH value. Thus, acidic conditions promote generation of hydroxyl radicals and degradation efficiency by lowering recombination reaction (Zhang et al. 2014).

Figure 8a and b showed the self-photodegradation of MB and MO, respectively. MB and MO was irradiated under xenon arc lamp for 30 min and analyzed using UV-vis spectroscopy at 664 nm and 464 nm for MB and MO, respectively. It was observed that there is no significant change in the MB and MO concentration. This showed that the direct photocatalysis or self-photodegradation was insignificant in the absence of the photocatalyst.

Figure 9 showed degradation efficiency vs time plot for degradation of MB, MO, and reduction of Cr(VI) in the presence of MSE5 and MSE8. Solutions of 1 mg/100 ml of each MB, MO, and Cr(VI) were prepared, and 20 mg of MSE5 and MSE8 were added to each solution and stirred under AM (air mass) 1.5 solar illuminations 100 mW/cm^2 from xenon arc lamp under same conditions. One milliliter of solution was taken out from each solution in some interval of time and analyzed using UV-visible spectroscopy. Degradation of MB, MO, and reduction of Cr(VI) into Cr(III) was observed by UV-Vis spectroscopy at characteristic absorbance peak at 664 nm, 464 nm, and 350 nm, respectively. $\eta = 1 - [C/C_0] * 100$ was used to calculate degradation efficiency (η), where C_0 denotes absorption of pollutant before irradiation and C denotes adsorption after irradiation at time t. MSE5 degraded 94.7% of MB, ∼ 92.6% of MO and ∼ 90.7% of Cr(VI) in 45 min of irradiation. MSE8 degraded 78% of MB, 77.8% of MO, and 66.7% of Cr(VI) in Cr(III) in 45 min of irradiation. As evident from the results (Fig. 9), MSE5 showed high photocatalytic efficiency as compared with MSE8 due to (i) enhanced surface area, (ii) high crystallinity, and (iii) large concentration of hydroxyl radicals. Enhanced surface area and large pore size in MSE5 as compared with MSE8 (Table 3) lead to increase in number of active sites, thus slower recombination rate and thereby producing more holes and electrons that help in degradation of adsorbed contaminants present on the surface of photocatalyst (Ashraf et al. 2019). Sample MSE5 has higher crystallinity as compared with MSE8 as evident through sharp and intense peaks observed in MSE5 through XRD and Raman studies (Figs. 3 and 4), resulting in higher degradation efficiency of MSE5 due to favorable charge transport properties. MSE5 has higher concentration of hydroxyl radicals as compared with MSE8 (Fig. 7g, h) which is a major reactant responsible for the degradation of pollutants.

Some of the earlier reported results of photodegradation of pollutants using $MoSe_2$, and its composites are summarized in Table 3. As observed from results, it can be seen that the degradation efficiency of MSE5 and MSE8 are higher for cationic dye, anionic dye as well as organic pollutant than those of other photocatalysts. Hence, MSE5 and MSE8 acted as an excellent photocatalyst.
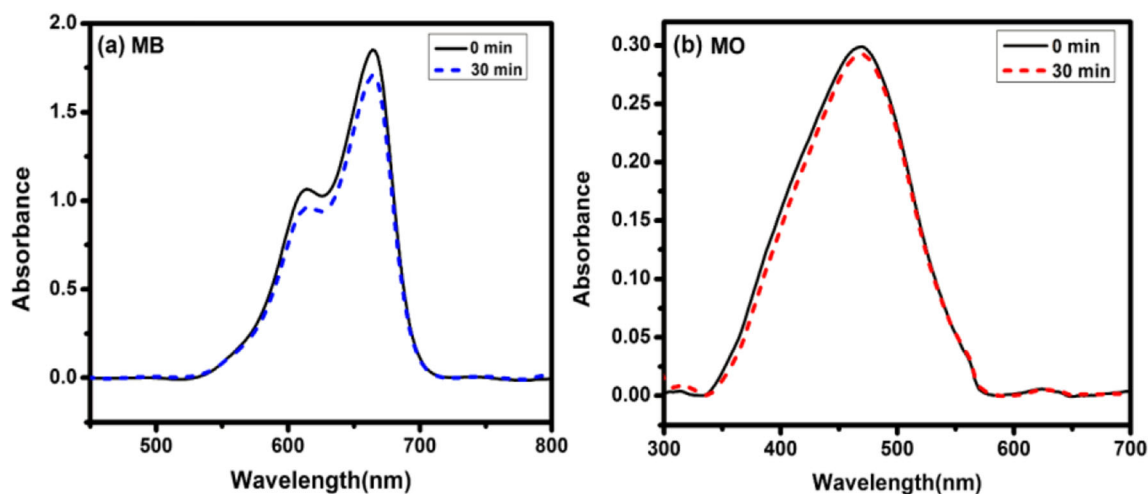

Fig. 8 Self- photodegradation of **a** MB and **b** MO using xenon lamp
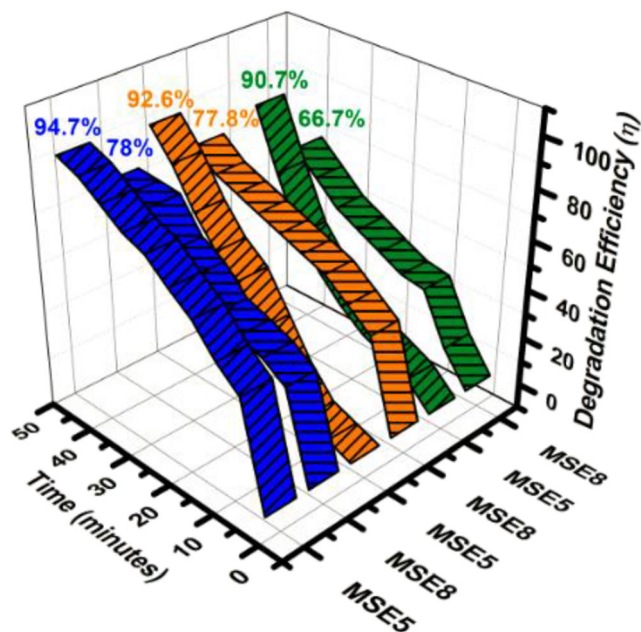
Fig. 9 Degradation efficiency vs time plot of MB, MO, and Cr(VI) in the presence of MSE5 and MSE8

Figure 10a and b showed C/C_0 vs time plot for degradation of MB, MO, and reduction of Cr(VI) in the presence of MSE5 and MSE8. Kinetics of adsorption on MSE5 and MSE8 were investigated by pseudo first order and pseudo second order as shown in Fig. 10.

The pseudo first-order adsorption, pseudo second-order adsorption and intra-particle diffusion model are given by the Eqs. (xiii) and (xiv), respectively.

$$Q_t = Q_e\left(1 - e^{-k_1 t}\right) \qquad (xiii)$$

$$\frac{t}{Q_t} = \frac{1}{k_2 (Q_e)^2} + \frac{t}{Q_e} \qquad (xiv)$$

where Q_t and Q_e denotes the adsorbed amount at time t and amount adsorbed at equilibrium. k_1 and k_2 are the rate constant for pseudo first order and pseudo second order, respectively. Values of k_1 and k_2 were evaluated from the slope of plot ln $(Q_e - Q_t)$ vs time and plot of t/Q_t vs time, respectively.

Kinetic study for MSE5 and MSE8 were found to follow pseudo first and second order adsorption model for MB, which suggested that adsorption process was initially controlled by physisorption followed by chemisorption. For MO and Cr(VI), MSE5 and MSE8 were found to follow pseudo first order adsorption model for MO and Cr(VI), which suggested that adsorption process was controlled by physisorption. In physisorption process, molecules form monolayer adsorption when adsorbed on the surface by valence bond. In chemisorption process, reaction between the surface and the adsorbate takes place. On interaction between the adsorbate molecule and surface of catalyst, in chemisorption process, new interacting electronic bonds, whereas in physisorption process no bond formation take place.

Table 3 Comparison of the photocatalytic degradation efficiency of MoSe$_2$ for different water pollutants

| Photocatalyst	Pollutant	Photodegradation efficiency (%)	Concentration of pollutant in water	References
MoSe$_2$/SrTiO$_3$	Methyl orange	99.46 at 75 min	20 mg/L	(Zhou et al. 2018)
MoSe$_2$/rGO	Methylene blue	98 at 180 min	15 mg/L	(Wu et al. 2016)
	Rhodamine B	98 at 180 min		
	Methyl orange	62.1 at 180 min		
MoSe$_2$ (flower-like)	Methyl orange	38 at 250 min	5–25 mg/L	(Tang et al. 2016)
C fibers@MoSe$_2$	Potassium dichromate	34.7 at 80 min	10 mg/L	(Wang et al. 2018)
	4-chlorophenol	19.4 at 80 min	5 mg/L	
MoSe$_2$ (nanoflowers)	Rhodamine B	99 at 10 min	10 ppm	(Jiang et al. 2017)
MoSe$_2$ (nanowire)	Rhodamine B	100 at 120 min	200 ppm	(Wu et al. 2017)
MoSe$_2$ (nanosheets) at pH 2	Chromium (VI)	100 at 180 min	80 mg/L	(Chu et al. 2016)
MoSe$_2$	Methylene blue	100 at 20 min	5 mg/L	(Siddiqui et al. 2018)
MoSe$_2$ (nanosheets)	Methylene blue	94.7 at 45 min	10 mg/L	This work
MoSe$_2$ (nanourchins)	Methyl orange	92.6 at 45 min	10 mg/L	
	Chromium(VI)	90.7 at 45 min	10 mg/L	
	Methylene blue	78 at 45 min	10 mg/L	
	Methyl orange	77.8 at 45 min	10 mg/L	
	Chromium(VI)	66.7 at 45 min	10 mg/L	
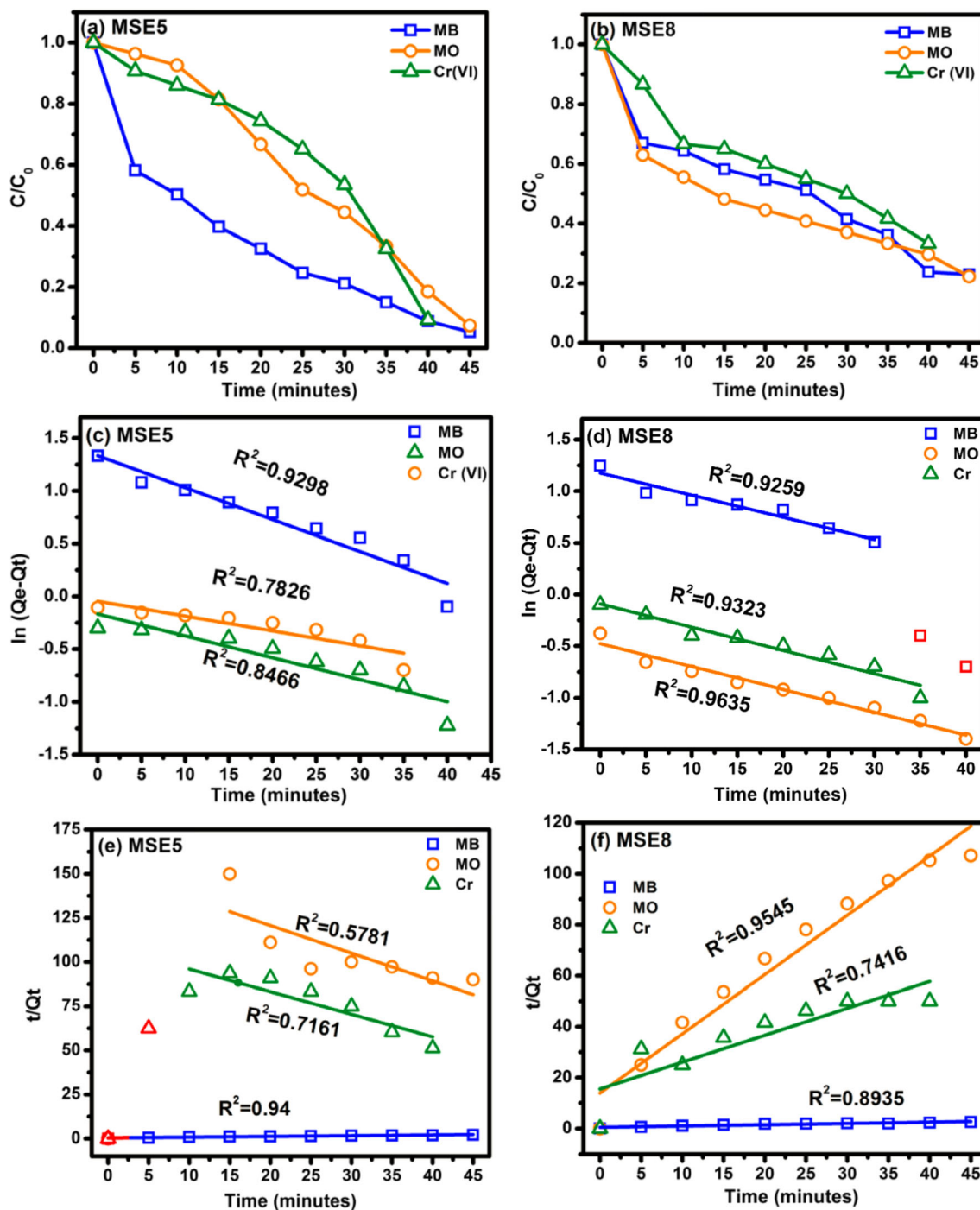
Fig. 10 **a**, **b** C/C_0 vs time plot **c**, **d** pseudo first order adsorption model and **e**, **f** pseudo second-order adsorption model of MB, MO, and Cr(VI)

In order to evaluate the reusability of MSE5 and MSE8, reduction of Cr(VI) into Cr(III) was checked for five cycles as shown in Fig. 11. In the first cycle, 92% and 67% of Cr(VI) was reduced using MSE5 and MSE8, respectively. The solutions resultant from the photocatalytic reduction was filtered washed and dried. The dried samples were used for the reduction of new solution of Cr(VI). After 5th cycle, degradation efficiency changed from 92 to 87% in case of MSE5 and 67 to

62% in case of MSE8. Such decrease was due to wastage of photocatalyst during each cycle and can be concluded that both photocatalyst acted as perfect candidate for environment remediation.

Photocatalytic degradation mechanism of $MoSe_2$ is shown in Fig. 12. Photocatalytic reaction initiated when irradiation light has energy equal to or greater than band gap of $MoSe_2$. Electrons from valence band moved to conduction band by
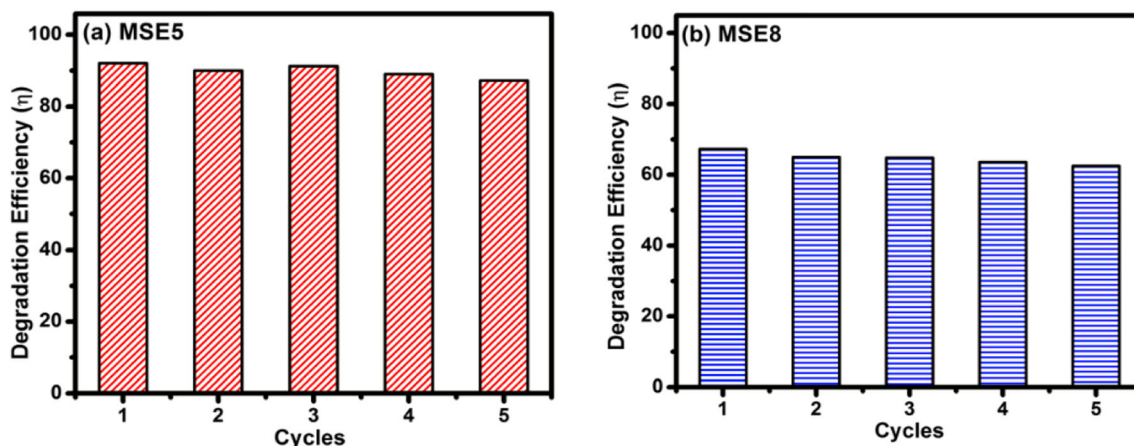
Fig. 11 Recyclability test of a MSE5 and b MSE8 for Cr(VI) reduction

absorbing energy from irradiation light, leaving behind a hole and resulting in formation of electron-hole pair. Holes reacts with water to yield hydroxyl radical, and electrons reacts with oxygen to yield superoxide radical which further produce hydroxyl radicals. These radicals react with contaminants and degrade them into harmless or less toxic substances.

Photocatalytic mechanism can be summarized as follows.

(a) Adsorption of photon- and electron-hole pair generation:

$$MoSe_2 + h\nu \rightarrow e^- + h^+ (MoSe_2-PANI) \quad (iv)$$
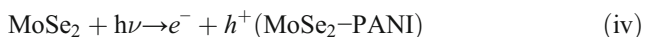
(b) Neutralization of OH^- groups to produce $^\bullet OH$ radicals:

$$H_2O \rightarrow OH^- + H^+ \quad (v)$$

$$h^+ + OH^- \rightarrow {}^\bullet OH \quad (vi)$$

(c) Oxygen ionosorption:

$$e^- + O_2 \rightarrow \cdot O_2^- \quad (vii)$$

(d) Neutralization of $\cdot O_2^-$ by protons:

$$\cdot O_2^- + H^+ \rightarrow HO_2^- \quad (viii)$$

(e) Transient hydrogen peroxide formation:

$$2HO_2^- \rightarrow O_2 + H_2O_2 \quad (ix)$$

(f) Second reduction of oxygen by H_2O_2

$$H_2O_2 + e^- \rightarrow OH^- + {}^\bullet OH \quad (x)$$

(g) Decomposition of contaminant by $^\bullet OH$ radical

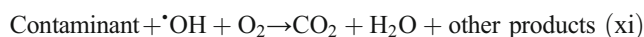$$Contaminant + {}^\bullet OH + O_2 \rightarrow CO_2 + H_2O + other\ products \quad (xi)$$
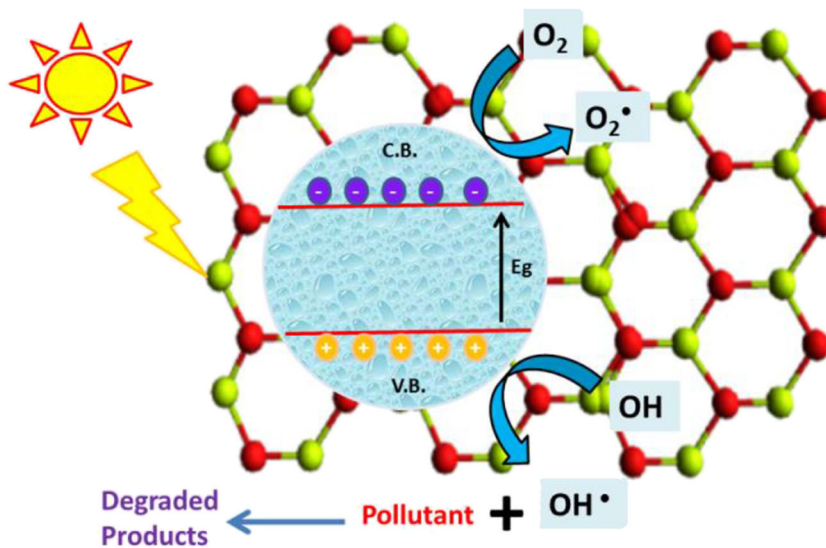
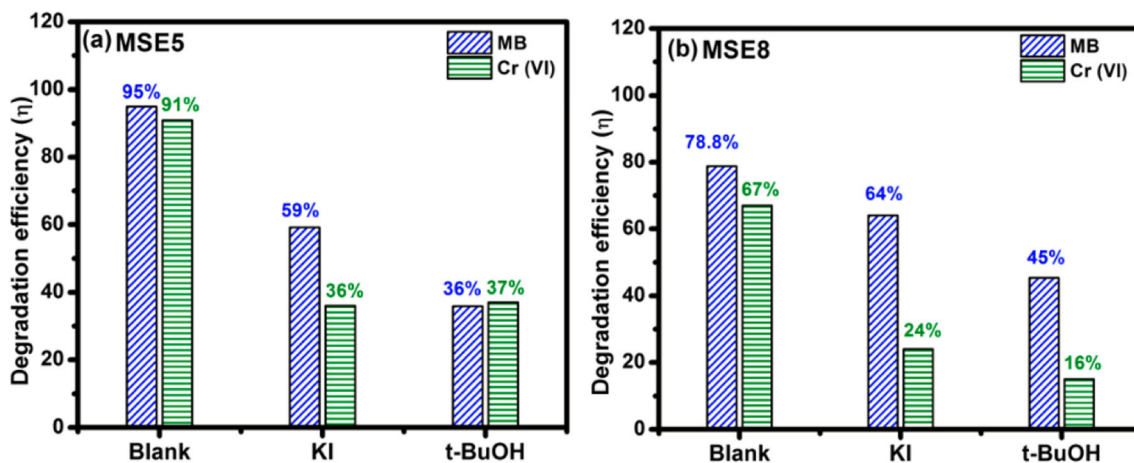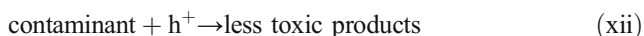Fig. 12 Photocatalytic mechanism of MoSe$_2$ nanostructures

Fig. 13 Trapping experiment for MB degradation and Cr(VI) reduction using t-BuOH and KI as scavengers in the presence of **a** MSE5 and **b** MSE8

(h)   Direct oxidation by holes

$$\text{contaminant} + h^+ \rightarrow \text{less toxic products} \qquad (xii)$$

In order to investigate the role of the reactive species in photocatalytic degradation mechanism, photocatalytic degradation of MB and reduction of Cr(VI) was performed in the presence of trappers such as t-BuOH for $^{\bullet}OH$ and KI for holes and $^{\bullet}OH$. 1mM in 100ml of t-BuOH and KI were used in the photocatalysis process (Mavinakere Ramesh and

Shivanna 2018; Mittal et al. 2019). Effect of radical trappers on the photodegradation efficiency of MSE5 and MSE8 is shown in Fig. 13. Reduction in photocatalytic activity was observed in the presence of trappers, implying the role of $^{\bullet}OH$ in the photodegradation process.

To investigate the degradation products of MB, HPLC was performed at 0 min and 30 min as shown in Fig. 14a and b, respectively. It was indicated from the results that photocatalytic degradation of dye not only caused its decoloration but also degraded the dye molecules. As shown in Fig. 14, intensity of MB peak was decreased, and new peaks appeared which corresponded to degraded products of the dye. Area of MB peak at 5.7 min decreased after 30 min, and new peaks at lower retention time were observed. Intermediates were observed at 2.0, 2.9, 3.2, and 3.5 min were assigned to thionin, azure C (AC), azure A (AA), and azure B (AB), respectively (Alamo-Nole et al. 2013; Ullah et al. 2017). These intermediates were further degraded and finally converted to CO_2 and H_2O.
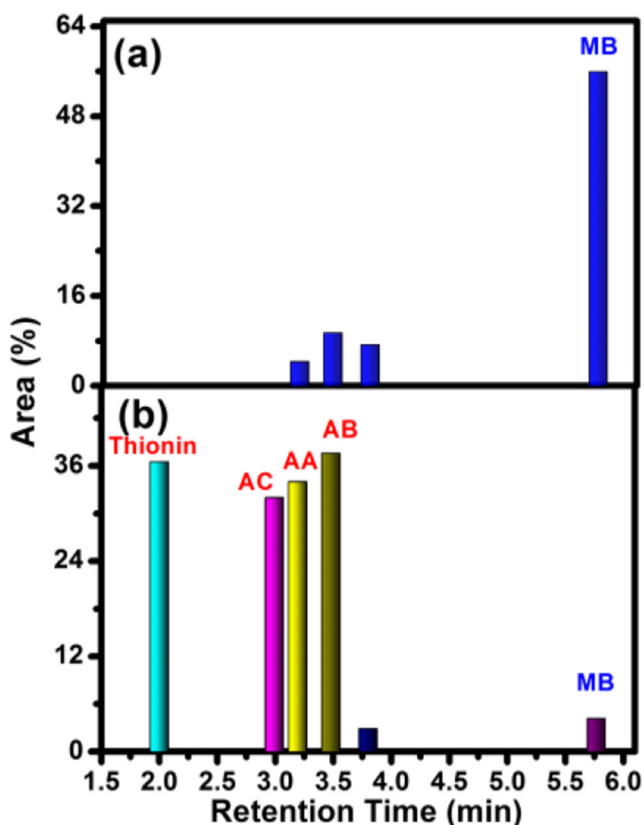
Conclusion

Nanosheets and nanourchins morphology of $MoSe_2$ were successfully obtained via hydrothermal method. During the synthesis process, acetic acid plays an important role in modification of the inherent negatively charged $MoSe_2$ surface. The photocatalytic degradation of cationic dye (MB), anionic dye (MO), and reduction of (Cr(VI)) using different morphologies of $MoSe_2$ (nanosheets and nanourchins) were performed and found to have good photocatalytic performance for cationic as well as anionic dye. The superior degradation efficiency of MSE5 (nanosheets) and MSE8 (nanourchins) is due to (i) high crystallinity of material (as observed by XRD and Raman studies), (ii) large pore size (as observed in BET analysis), and (iii) higher concentration of $^{\bullet}OH$ radicals (as observed by XPS studies). The degraded products of MB were examined by high-performance liquid chromatography (HPLC) which confirms

Fig. 14 HPLC analysis of degraded products of MB at **a** 0 min and **b** 30 min using MSE5

the complete degradation of dye. Photocatalysis mechanism along with trapping experiment was explained. Reaction kinetics were studied and found to follow pseudo first- and second-order model. Repeatability of the materials were also studied and found to have reusable properties.

References

Alamo-Nole L, Bailon-Ruiz S, Luna-Pineda T, Perales-Perez O, Roman FR (2013) Photocatalytic activity of quantum dot–magnetite nanocomposites to degrade organic dyes in the aqueous phase. J Mater Chem A 1:5509–5516

Andoshe DM, Jeon J-M, Kim SY, Jang HW (2015) Two-dimensional transition metal dichalcogenide nanomaterials for solar water splitting. Electron Mater Lett 11:323–335

Ashraf W, Fatima T, Srivastava K, Khanuja M (2019) Superior photocatalytic activity of tungsten disulfide nanostructures: role of morphology and defects. Appl Nanosci 1–15. https://doi.org/10.1007/s13204-019-00951-4

Azeez F, Al-Hetlani E, Arafa M, Abdelmonem Y, Nazeer AA, Amin MO, Madkour M (2018) The effect of surface charge on photocatalytic degradation of methylene blue dye using chargeable titania nanoparticles. Sci Rep 8:7104

Bhuyan T, Mishra K, Khanuja M, Prasad R, Varma A (2015) Biosynthesis of zinc oxide nanoparticles from Azadirachta indica for antibacterial and photocatalytic applications. Mater Sci Semicond Process 32:55–61

Bi E, Chen H, Yang X, Ye F, Yin M, Han L (2015) Fullerene-structured MoSe₂ hollow spheres anchored on highly nitrogen-doped graphene as a conductive catalyst for photovoltaic applications. Sci Rep 5:13214

Chaudhary N, Khanuja M, Islam S (2018) Hydrothermal synthesis of MoS₂ nanosheets for multiple wavelength optical sensing applications. Sensors Actuators A Phys 277:190–198

Chu H, Liu X, Liu B, Zhu G, Lei W, du H, Liu J, Li J, Li C, Sun C (2016) Hexagonal 2H-MoSe₂ broad spectrum active photocatalyst for Cr (VI) reduction. Sci Rep 6:35304

Fan C, Wei Z, Yang S, Li J (2014) Synthesis of MoSe₂ flower-like nanostructures and their photo-responsive properties. RSC Adv 4:775–778

Gągol M, Przyjazny A, Boczkaj G (2018) Wastewater treatment by means of advanced oxidation processes based on cavitation—a review. Chem Eng J 338:599–627

Ghosh R, Kim J-S, Roy A, Chou H, Vu M, Banerjee SK, Akinwande D (2016) Large area chemical vapor deposition growth of monolayer MoSe 2 and its controlled sulfurization to MoS₂. J Mater Res 31:917–922

Harpeness R, Gedanken A, Weiss A, Slifkin M (2003) Microwave-assisted synthesis of nanosized MoSe₂. J Mater Chem 13:2603–2606

Huang J, Liu H, Jin B, Liu M, Zhang Q, Luo L, Chu S, Chu S, Peng R (2017) Large-area snow-like MoSe₂ monolayers: synthesis, growth mechanism, and efficient electrocatalyst application. Nanotechnology 28:275704

Jia L, Sun X, Jiang Y, Yu S, Wang C (2015) A novel MoSe₂–reduced graphene oxide/polyimide composite film for applications in electrocatalysis and photoelectrocatalysis hydrogen evolution. Adv Funct Mater 25:1814–1820

Jiang Q, Lu Y, Huang Z, Hu J (2017) Facile solvent-thermal synthesis of ultrathin MoSe₂ nanosheets for hydrogen evolution and organic dyes adsorption. Appl Surf Sci 402:277–285

Khanuja M, Kala S, Mehta BR, Sharma H, Shivaprasad SM, Balamurgan B, Maisels A, Kruis FE (2007) XPS and AFM studies of monodispersed Pb/PbO core–shell nanostructures. J Nanosci Nanotechnol 7:2096–2100

Khanuja M, Mehta B, Shivaprasad S (2008) Two approaches for enhancing the hydrogenation properties of palladium: metal nanoparticle and thin film over layers. J Chem Sci 120:573–578

Kirubasankar B, Palanisamy P, Arunachalam S, Murugadoss V, Angaiah S (2019) 2D MoSe₂-Ni (OH)₂ nanohybrid as an efficient electrode material with high rate capability for asymmetric supercapacitor applications. Chem Eng J 355:881–890

Ko YN, Choi S, Park S, Kang YC (2014) Hierarchical MoSe₂ yolk–shell microspheres with superior Na-ion storage properties. Nanoscale 6:10511–10515

Liu Y, Zhu M, Chen D (2015) Sheet-like MoSe₂/C composites with enhanced Li-ion storage properties. J Mater Chem A 3:11857–11862

Mavinakere Ramesh A, Shivanna S (2018) Visible light assisted photocatalytic degradation of chromium (VI) by using nanoporous Fe₂O₃. J Mater 2018. https://doi.org/10.1155/2018/1593947

Mittal H, Kumar A, Khanuja M (2019) In-situ oxidative polymerization of aniline on hydrothermally synthesized MoSe₂ for enhanced photocatalytic degradation of organic dyes. J Saudi Chem Soc. https://doi.org/10.1016/j.jscs.2019.02.004

Narang J, Mishra A, Pilloton R, VV A, Wadhwa S, Pundir C, Khanuja M (2018a) Development of MoSe₂ nano-urchins as a sensing platform for a selective bio-capturing of Escherichia coli shiga toxin DNA. Biosensors 8:77

Narang J, Singhal C, Khanuja M, Mathur A, Jain A, Pundir C (2018b) Hydrothermally synthesized zinc oxide nanorods incorporated on lab-on-paper device for electrochemical detection of recreational drug. Artif Cells Nanomed Biotechnol 46:1586–1593

Poh SM, Tan SJR, Zhao X, Chen Z, Abdelwahab I, Fu D, Xu H, Bao Y, Zhou W, Loh KP (2017) Large area synthesis of 1D-MoSe₂ using molecular beam epitaxy. Adv Mater 29:1605641

Roy A, Movva HCP, Satpati B, Kim K, Dey R, Rai A, Pramanik T, Guchhait S, Tutuc E, Banerjee SK (2016) Structural and electrical properties of MoTe₂ and MoSe₂ grown by molecular beam epitaxy. ACS Appl Mater Interfaces 8:7396–7402

Saha S, Chaudhary N, Mittal H, Gupta G, Khanuja M (2019) Inorganic–organic nanohybrid of MoS₂-PANI for advanced photocatalytic application. Int Nano Lett 1–13. https://doi.org/10.1007/s40089-019-0267-5

Salem MA, Al-Ghonemiy AF, Zaki AB (2009) Photocatalytic degradation of Allura red and Quinoline yellow with Polyaniline/TiO₂ nanocomposite. Appl Catal B: Environ 91:59–66

Sharma R, Khanuja M, Islam S, Singhal U, Varma A (2017) Aspect-ratio-dependent photoinduced antimicrobial and photocatalytic organic pollutant degradation efficiency of ZnO nanorods. Res Chem Intermed 43:5345–5364

Shi H, Zhou X, Lin Y, Fu X (2008) Synthesis of MoSe₂ nano-flakes modified with dithiophosphinic acid extractant at low temperature. Mater Lett 62:3649–3651

Shrivastava V (2012) Photocatalytic degradation of methylene blue dye and chromium metal from wastewater using nanocrystalline TiO₂ semiconductor. Arch Appl Sci Res 4:1244–1254

Siddiqui I, Mittal H, Kohli VK, Gautam P, Ali M, Khanuja M (2018) Hydrothermally synthesized micron sized, broom-shaped MoSe₂ nanostructures for superior photocatalytic water purification. Mater Res Exp 5:125020

Singh S, Pendurthi R, Khanuja M, Islam S, Rajput S, Shivaprasad S (2017) Copper-doped modified ZnO nanorods to tailor its light assisted charge transfer reactions exploited for photo-electrochemical and photo-catalytic application in environmental remediation. Appl Phys A 123:184

Singh S, Sharma R, Khanuja M (2018) A review and recent developments on strategies to improve the photocatalytic elimination of organic dye pollutants by BiOX (X=Cl, Br, I, F) nanostructures. Korean J Chem Eng 35:1955–1968

Tang H, Huang H, Wang X, Wu K, Tang G, Li C (2016) Hydrothermal synthesis of 3D hierarchical flower-like $MoSe_2$ microspheres and their adsorption performances for methyl orange. Appl Surf Sci 379:296–303

Toor M, Jin B (2012) Adsorption characteristics, isotherm, kinetics, and diffusion of modified natural bentonite for removing diazo dye. Chem Eng J 187:79–88

Ullah AA, Kibria AF, Akter M, Khan M, Tareq A, Firoz SH (2017) Oxidative degradation of methylene blue using Mn_3O_4 nanoparticles. Water Conserv Sci Eng 1:249–256

Wang B, Ostrikov K, Van Der Laan T, Zheng K, Shao R, Zhu M, Zou S (2016) Growth and photoluminescence of oriented $MoSe_2$ nanosheets produced by hot filament CVD. RSC Adv 6:37236–37245

Wang M, Peng Z, Qian J, Li H, Zhao Z, Fu X (2018) Highly efficient solar-driven photocatalytic degradation on environmental pollutants over a novel C fibers@ $MoSe_2$ nanoplates core-shell composite. J Hazard Mater 347:403–411

Wu Y, Xu M, Chen X, Yang S, Wu H, Pan J, Xiong X (2016) CTAB-assisted synthesis of novel ultrathin $MoSe_2$ nanosheets perpendicular to graphene for the adsorption and photodegradation of organic dyes under visible light. Nanoscale 8:440–450

Wu M-H, Lee J-T, Chung YJ, Srinivaas M, Wu J-M (2017) Ultrahigh efficient degradation activity of single-and few-layered $MoSe_2$ nanoflowers in dark by piezo-catalyst effect. Nano Energy 40:369–375

Zhang J, Nosaka Y, (2014) Mechanism of the OH radical generation in photocatalysis with TiO_2 of different crystalline types. J Phys Chem 118 (20):10824-10832

Zhan J, Zhang Z, Qian X, Xie CWY, Qian Y (1999) Synthesis of $MoSe_2$ nanocrystallites by a solvothermal conversion from MoO_3. Mater Res Bull 34:497–501

Zhang Y, Gong Q, Li L, Yang H, Li Y, Wang Q (2015) $MoSe_2$ porous microspheres comprising monolayer flakes with high electrocatalytic activity. Nano Res 8:1108–1115

Zhang C, Chen X, Peng Z, Fu X, Lian L, Luo W, Zhang J, Li H, Wang YH, Zhang D (2018) Phosphine-free synthesis and shape evolution of $MoSe_2$ nanoflowers for electrocatalytic hydrogen evolution reactions. CrystEngComm 20:2491–2498

Zhao X, Sui J, Li F, Fang H, Wang H, Li J, Cai W, Cao G (2016) Lamellar $MoSe_2$ nanosheets embedded with MoO_2 nanoparticles: novel hybrid nanostructures promoted excellent performances for lithium ion batteries. Nanoscale 8:17902–17910

Zhou X, Jiang J, Ding T, Zhang J, Pan B, Zuo J, Yang Q (2014) Fast colloidal synthesis of scalable Mo-rich hierarchical ultrathin $MoSe_{2-x}$ nanosheets for high-performance hydrogen evolution. Nanoscale 6:11046–11051

Zhou X, Yao J, Yang M, Ma J, Zhou Q, Ou E, Zhang Z, Sun X (2018) Synthesis of $MoSe_2/SrTiO_3$ heterostructures with enhanced ultraviolet-light-driven and visible-light-driven photocatalytic properties. Nano 13:1850038